

Contents lists available at ScienceDirect

Spectrochimica Acta Part B: Atomic Spectroscopy

journal homepage: www.elsevier.com/locate/sab





Elemental fractionation in aerosol laser-induced breakdown spectroscopy with nanosecond and femtosecond laser ablation

Kyle S. Latty*, Kyle C. Hartig

Nuclear Engineering Program, Department of Materials Science and Engineering, University of Florida, Gainesville, FL 32611, USA

ARTICLE INFO

Keywords:
Cesium
Aerosol
Laser-induced breakdown spectroscopy
Matrix effect
Elemental fractionation

ABSTRACT

For the purpose of realizing atmospheric radiation plume tracking, laser-induced breakdown spectroscopy (LIBS) was performed to characterize Cs atomic emissions from airborne nanoparticles in a binary particle matrix using nanosecond and femtosecond laser ablation. As a surrogate to multi-element nuclear fallout particulates, both Cs and Na solutions were mixed with Cu at a 1:1.45 M concentration ratio and aerosolized to study elemental fractionation in atomic emissions, revealing Na I resonance emissions are enhanced whereas Cs I resonance emissions are reduced with Cu present despite sharing similar electronic and chemical properties. Femtosecond laser ablation reduced elemental fractionation effects by more than 50% while retaining the same temporal fractionation trends for Cs and Na. The origin of elemental fractionation in aerosol LIBS was further investigated using Al and Ti aerosols which revealed that the particle matrix induces changes to the local plasma temperature, population of atomic states, and subsequent molecular association and emission.

1. Introduction

An estimated total activity of several petabecquerel (PBq) was released into the atmosphere as a result of the Fukushima Daiichi Nuclear Power Plant accident in March of 2011, which mostly consisted of fission gases and particles composed of volatile fission elements [1,2]. Similar estimates were made for the Chernobyl accident in April of 1986, where the total activity released is regularly reported to be an order of magnitude greater in comparison to the Fukushima accident [3,4]. For both accidents, the resulting radioactive gases and aerosols traveled continental distances where increases in local airborne radiation activity levels were internationally reported [5–7].

In the event of a catastrophic nuclear release, the capability to rapidly detect and track the resulting atmospheric radiation plume is necessary to avoid contamination to critical assets and minimize exposure to emergency personnel. In the past, laser-induced breakdown spectroscopy (LIBS) has been used to measure both actinide [8,9] and fission product [10,11] emissions from a laser-produced plasma (LPP). Furthermore, the ability to perform remote LIBS and standoff measurements through filament-induced breakdown spectroscopy (FIBS) without the need for sample preparation or sample contact is highly desirable as it minimizes exposure where radioactive or other facility hazards are present [12,13]. However, realizing atmospheric plume

tracking using LIBS presents difficult challenges, among them being matrix effects associated with particle size distributions and multi-element composition of particles.

Unlike bulk, solid sample measurements with LIBS where the lasersample interaction dictates most of the plasma evolution, aerosol LIBS is performed by forming LPPs in air which most frequently dissociates the entrained particle mass through plasma-particle interactions instead of direct laser interactions [14]. The thermally driven dissociation process is described to be rate-limited such that the rate of vaporization of particle mass is comparable to the analytical measurement time [15]. Particles larger than 2.1 µm have been found to undergo incomplete dissociation in the plasma giving rise to a particle-size matrix effect, where different upper size limits have been reported depending on the particle composition [16,17]. A disproportion between the analyte mass and the subsequent emission results from the matrix effect, reducing quantitative capabilities for particle sizes exceeding the complete dissociation limit. The size of particles derived from nuclear detonations and reactor-based accidents is highly correlated to the distance from the release source, where larger microparticles are found closer to the source due to faster settling velocities [18-21]. As such, the prominence of the particle size matrix effect can be reduced by performing measurements distanced from the release site where nanometer particle size distributions predominate.

E-mail address: klatty@ufl.edu (K.S. Latty).

^{*} Corresponding author.

Elemental fractionation is a matrix effect that has been observed to occur in LIBS when measuring multi-element aerosols where analyte emissions are influenced by the particle matrix. A similar phenomenon is known to occur in laser ablation (LA)-based mass spectrometry methods, where non-stoichiometric effects arise due to differences in laser ablation, material transport, and inductively-coupled plasma excitation and ionization occurs based on the sample matrix [22–24]. Here, a large contribution to elemental fractionation is determined to be due to differences in ablation conditions such that highly volatile elements are preferentially vaporized in the sample. As such, the use of fs-LA has gained popularity where thermal effects that drive vaporization are reduced which has been shown to limit elemental fractionation [25,26].

Elemental fractionation in aerosol LIBS was first observed by Diwakar et al. when measuring binary Na:Cu dry aerosols at a 1:9 mass ratio [27]. A 50% enhancement in Na I doublet emissions in the early stages of the plasma was observed when mixed with Cu, Zn, and W. The authors attributed the enhancement to the range of volatility of the explored elements which was speculated to perturb local plasma conditions depending on the mass composition of the aerosol particles. The authors assumed the local plasma temperature is being suppressed with concomitant species present which reduces the Na II-to-Na I ratio under local thermodynamic equilibrium (LTE), resulting in enhanced Na I emissions [28]. The local plasma temperature was determined using Saha-Boltzmann equations for Mg and Cd where temperature was shown to increase from 0–40 μ s, which the authors attributed to the slow rate of heat transfer from the plasma into the particle.

The temperature and electron density of particle and bulk (i.e. surrounding gas) species are further explored by Asgill et al. where particlederived temperatures were extracted for Lu II, Mg II, and Mn I and bulk plasma temperatures were extracted from ambient gases including Ar II, N II, and N I using Boltzmann plots [29]. The particle matrix is confirmed to be multi-element mixture of Lu, Mg, and Al using transmission electron microscopy (TEM) and energy-dispersive X-ray spectroscopy (EDS), where particles sizes are confirmed to remain under 1 μm. The local plasma temperature determined from Mn II was lower compared to Lu II which is attributed to the lower ionization threshold of Lu leading to temperature suppression, similar to the conclusion drawn by Diwakar et al., although a similar increase in local plasma temperature was not observed [27]. While electron densities were determined from gaseous H and Ar, the inability to obtain particle-derived electron densities limited further analysis. The addition of Na to the particle matrix was shown to slightly influence the the local plasma temperature but not enough to result in statistical significance.

A theoretical and experimental investigation on the origins of elemental fractionation in LIBS was performed by Judge et al. using binary Na and Cu pressed pellets [30]. Like with aerosols, the measurements showed an enhancement in the Na I doublet emissions with Cu present where similar temporal trends in the signal enhancement found by Diwakar et al. was replicated [27]. The experimental data was simulated under LTE conditions at a constant temperature and plasma mass density using ATOMIC, an atomic and plasma physics code developed by Los Alamos National Laboratory [31]. Theoretical simulations indicated the electron density is being increased as the molar ratio of Cu was increased relative to Na, where pure Na resulted in an electron density of $1.3\times10^{16}~\text{cm}^{-3}$ which increased to $3.2\times10^{16}~\text{cm}^{-3}$ at a 1:9 Na:Cu molar ratio. The authors conclude that the increase in electron density drives higher neutral atom recombination rates which results in enhanced Na I emissions. The measurements also showed that the Mg I emission are enhanced whereas Mg II emissions are reduced with Cu present, which is indicated to support a shift in the neutral-toion ratio.

The discussed investigations into aerosol LIBS elemental fractionation [27,29,30] all hint at the significance of elemental volatility and ionization thresholds, where inclusion of concomitant species in some ways perturb the plasma properties that results in spectroscopic changes. This is a crucial point of investigation for quantitative LIBS

applications involving fission product in nuclear fallout particles, where nanoparticles are typically rich in volatile fission product elements such as Cs, I, Sr, and Ba [4]. The exact mechanism driving elemental fractionation in aerosol LIBS remains unknown which currently stands to hinder quantitative capabilities. And while LA-based mass spectrometry methods have shown fs-LA to reduce matrix effects [22–24], the potential alterations on aerosol LIBS matrix effects are yet to be explored. A change in fractionation behavior should arise given plasma-particle interactions are highly dependent on the overall LPP characteristics which are distinctly different between fs-LPPs and ns-LPPs in air.

In this work, the Na I signal enhancement that is known to occur in a binary Na:Cu mixture is verified and further investigated using Cs as an alkali metal substitute for Na. Of all elements, Cs has the lowest first ionization threshold and is a highly volatile alkali metal which serves to elucidate the role of both ionization thresholds and volatility on elemental fractionation. Short-focused (SF) fs-pulses are used in order to observe potential alterations to fractionation trends for Na and Cs. Strong emissions lines for both Na and Cs were primarily limited to their resonance doublet emissions which are prone to self-absorption under current experimental conditions, and thus particle-derived local plasma temperatures and electron densities are determined using binary Al:Ti aerosols. Both Al and Ti have prominent monoxide emissions (i.e. TiO and AlO) in the visible wavelength region such that molecular formation can be investigated through LIBS as a potential contributor to elemental fractionation in volatile elements.

2. Experimental setup and methods

A simplified schematic of the aerosol LIBS experimental setup is provided in Fig. 1. For all ns-LIBS measurements, a Q-switched Nd:YAG laser (Continuum Surelite II) with a fundamental wavelength of 1064 nm, repetition rate of 10 Hz, pulse duration of 6 ns, and beam diameter of 13 mm is used with a reduced pulse energy of 255 mJ after beam expansion. A chirp-pulse amplified Ti:Sapphire laser (Coherent Astrella USP) with a central wavelength of 800 nm, pulse duration of 35 fs, repetition rate of 1 kHz, pulse energy of 6.8 mJ, and beam diameter of 10 mm is used for fs-LIBS experiments. Pulse energies for both lasers do not deviate by more than 0.8%, and are focused using a D = 25.4 mm and f = 75 mm BK7 lens. With a 75 mm focusing lens, filamentation is avoided such that electron densities exceed intensity-clamped limits which generates an intense LPP in air [32].

Laser produced plasma emissions are collected orthogonal to the beam path using a D =25.4 mm and f =75 mm uncoated UV fused-silica lens and coupled with a multimode fiber (Ø 1.3 mm) into a Czerny-Turner spectrometer (Princeton Instruments HRS-500) mated to an emICCD (Princeton Instruments PI-MAX4) camera to perform time-resolved LIBS measurements. Due to self-focusing and chromatic aberrations in the BK7 lens, the fs-pulse focuses earlier with relation to the

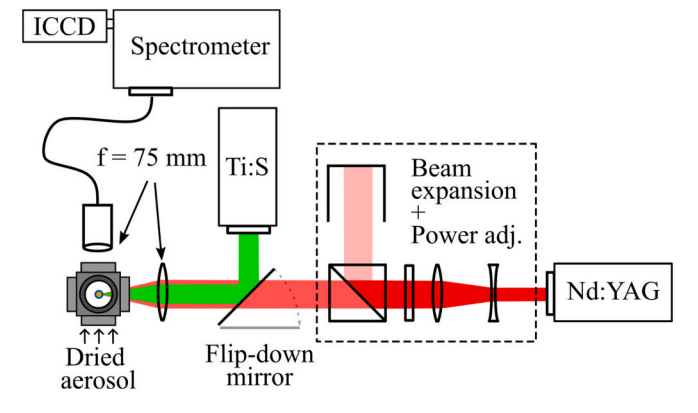


Fig. 1. Experimental setup for laser-induced breakdown spectroscopy of dry aerosols. Collection optics placed orthogonal to beam path.

ns-pulse such that realignment of the collection optics is necessary. All measurements are taken with the collection lens focused 5 mm before the plasma center to better couple emissions representative of bulk plasma conditions where the plasma is approximately 1.5–2 mm in diameter [33,34]. A 1200 gr/mm grating is used for Na, Cs, and Cu measurements and a 2400 gr/mm grating is used for Al and Ti measurements where the spectral resolution for the 1200 gr/mm and 2400 gr/mm gratings are measured to be 0.09955 nm and 0.04974 nm using a Hg lamp at 435.835 nm, respectively. Measurements for Ti are corrected for wavelength dependent instrumental response changes using a calibrated tungsten halogen lamp (Ocean Insight HL-3P-CAL) to construct Boltzmann plots.

Dry aerosols are produced through a custom 3D printed drying apparatus that mixes a dry air co-flow with an aqueous aerosol mist to encourage droplet desolvation and is based off the design reported by Hahn et al. in [35]. The dry aerosol is flowed through an enclosed sixway sampling chamber attached with a laser window, a viewing window, and an overhead exhaust to collect airborne particles with a HEPA filter for later disposal. The aqueous aerosol is aspirated at a rate of 0.09 mL/min using a 6 L/min gas flow rate using a medical nebulizer (Resperonics SideStream) with a droplet mean aerodynamic diameter specified at \approx 3.1 µm by the manufacturer. The co-flow is set to 60 L/min for aerosols containing Na, Cs, and Cu, and reduced to 10 L/min for aerosols containing Al and Ti to improve the weaker emissions from AlO and TiO by increasing the mass concentration of the aerosol in the sampling chamber. Droplet desolvation is confirmed using speckled light from a HeNe laser for all flow rates used in this study. Certified 10,000 μg/mL inductively-coupled plasma (ICP) standard solutions (SPEX CertiPrep) are used to produce single and binary aerosols listed in Table 1 and diluted to achieve desired molar concentrations and ratios. The lowest molar concentration used is set to 43.47 mols/mL for Na, Cs, and Al corresponding to a relatively high particle concentration such that single-shot conditional analysis is unnecessary [36,37].

3. Results and discussion

3.1. Na and Cs mixed with Cu

Aerosol LIBS emissions are quantified by extracting the amplitude from a normalized Voigt profile to lines of interest such that reported values are integrated quantities of the area under the line profile and is independent of the background signal. Each aerosol is measured using five subsequent 300 shot averages which are fitted independently to produce one standard deviation error bars. Elemental fractionation is described through the fractionation ratio which is defined as the ratio of the integrated intensity of a given emission line with the binary aerosol (*i.e.*, Na:Cu, Cs:Cu, Al:Ti) to the integrated intensity of the same emission line with one of the single element aerosols (*i.e.*, Na, Cs, Al, etc.). For example, the fractionation ratio for Na with Cu is the integrated intensity of a Na emission line for the Na:Cu aerosol (see Table 1) over the integrated intensity of the same Na emission line for a pure Na aerosol of equal concentration.

In previous studies, the emissions from the Na I doublet at 588.995 nm and 588.995 nm was shown to be enhanced in the presence of Cu for

Table 1
Aerosolized solutions investigated in this work.

sol.1: sol.2	sol.1 conc. (μg/mL)	sol.2 conc. (μg/mL)	Molar ratio
Na: -	1000	_	_
Cs: -	5781	_	_
Cu: –	4000	_	_
Na: Cu	1000	4000	1: 1.45
Cs: Cu	5781	4000	1: 1.45
Al: -	1173	_	_
Ti: -	3013	_	_
Al: Ti	1173	3013	1: 1.45

both dry aerosols and pressed pellets [27,30]. Using the current experimental setup, a similar trend is recovered for Na at 588.995 nm where the signal is enhanced by approximately 30% with Cu using ns-LIBS with a decrease in enhancement at later times as shown in Fig. 2(a). Experiments by Diwakar et al. achieved approximately a 50% enhancement for Na and was also noted to remain relatively consistent for Na:Cu mass concentration ratios ranging from 1:1 to 1:9 which captures the 1:4 ratio currently being used [28]. The discrepancy in fractionation ratios is attributed to the differences in experimental methods including the flow rates, depth of focus of the collection lens, and gating settings which have been found to influence the fractionation ratio. While self-reversal is not observed, resonance lines are susceptible to self-absorption which also influences the fractionation ratio.

An opposite trend is observed for Cs at 852.113 nm as emissions are reduced by more than 30% when Cu is present. Both Na and Cs are alkali metals which share similar electronic structure and chemical behavior with most notable differences being the lower first ionization threshold (Na - 5.139 eV, Cs - 3.894 eV) and upper energy level (Na I 588.995 nm - 2.104 eV, Cs I 852.113 nm - 1.455 eV) of Cs compared to Na [38]. This manifests as longer-lived emissions for Cs as shown in Fig. 2(b) as the upper level energy states remain populated as the plasma cools towards later times. Conceivably, if emission enhancement arise due to higher neutral atom recombination rates through the addition Cu as indicated by Judge et al., Cs is expected to experience similar and if not greater signal enhancement compared to Na. The lower ionization threshold of Cs should theoretically contribute to a higher free electron population, and thus signal enhancement should be more prominent as more Cs ions

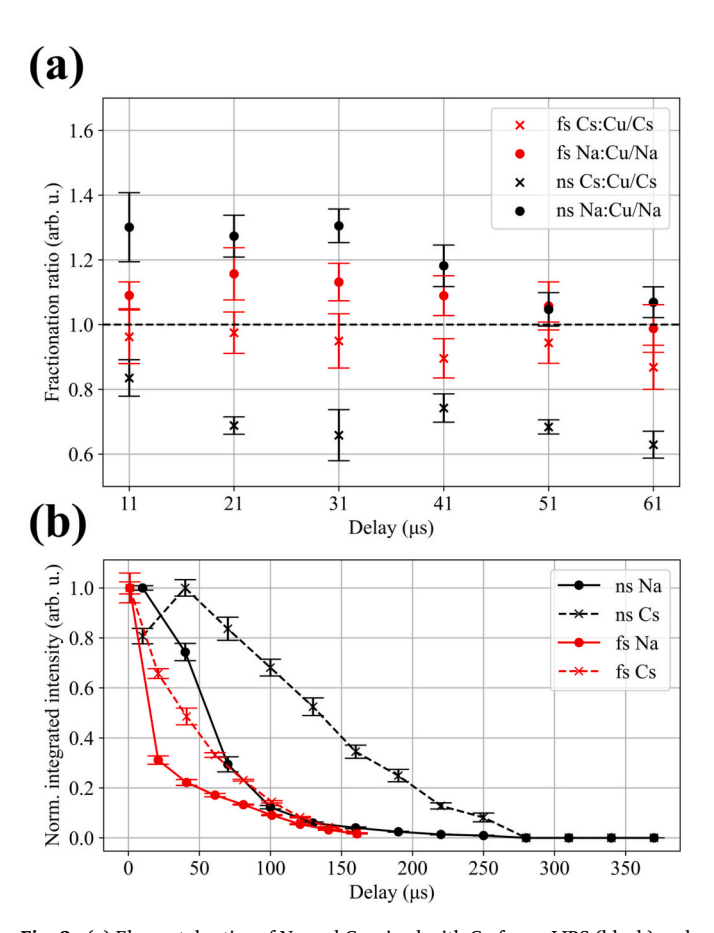


Fig. 2. (a) Elemental ratios of Na and Cs mixed with Cu for ns-LIBS (black) and fs-LIBS (red). ICCD gate delay stepped using 10 μs increments with a 10 μs gate width. (b) Emission behavior of Cs compared to Na using a fixed 30 μs gate width with 30 μs gate delay increments for ns-LIBS. A similar procedure is repeated for fs-LIBS using 20 μs increments. The 588.995 nm and 852.113 nm lines are used for Na and Cs, respectively.

undergo recombination compared to Na.

The severity of elemental fractionation is shown to be greatly reduced using fs-pulses in Fig. 2(a). The same trends as ns-LIBS is shown to persist using fs-LIBS where Na emissions are enhanced and Cs emission are reduced with Cu present. As with ns-LIBS, emissions from Cs are shown to persist into later stages of the plasma in Fig. 2(b) due to the low upper energy level of the resonance transition. Under the framework that particle dissociation is dictated by the plasma interacting with the particle [34,39], it stands to reason that elemental fractionation is driven mainly by the characteristics of the plasma including temperature, electron density, expansion, and recombination rates which are vastly different between ns-pulses and fs-pulses [40–42].

While Diwakar et al. [27] found the continuum emissions to remain unchanged with the addition of Cu, the presented experiments showed a predictable change in the early continuum based on enhancement or reduction as shown in Fig. 3. Signal enhancement is experienced by Na and thus there is a corresponding enhancement in the early continuum, whereas both Cs and Cu (Fig. 3 inset) experience signal reduction and thus a corresponding decrease in continuum emissions. The LIBS continuum is known to be a contribution from both free-free transitions (e. g., Bremmstruhlung) and free-bound transitions (e.g., radiative recombination), with the relative contributions of each being highly dependent on the plasma temperature relative to the ionization threshold of the plasma species [43]. This serves as a possible explanation to the reduced effects of elemental fractionation using fs-LIBS, where plasma temperatures are generally reported to be lower than ns-LIBS which also gives rise to a reduced continuum emissions [41,42]. The continuum is not considered to directly influence elemental fractionation, but serves as an indicator that the local plasma temperature is being changed based on the elemental composition of the aerosol.

3.2. Al and Ti mixtures

In order to investigate particle-derived temperatures, the Ti and Al:Ti aerosols detailed in Table 1 are used which provided better upper energy level distributions for Boltzmann plots compared to the Cu aerosols. The Ti lines used for the Boltzmann plots are provided in Table 2, which spans the upper energy levels from 2.396 eV to 4.808 eV. Time-resolved

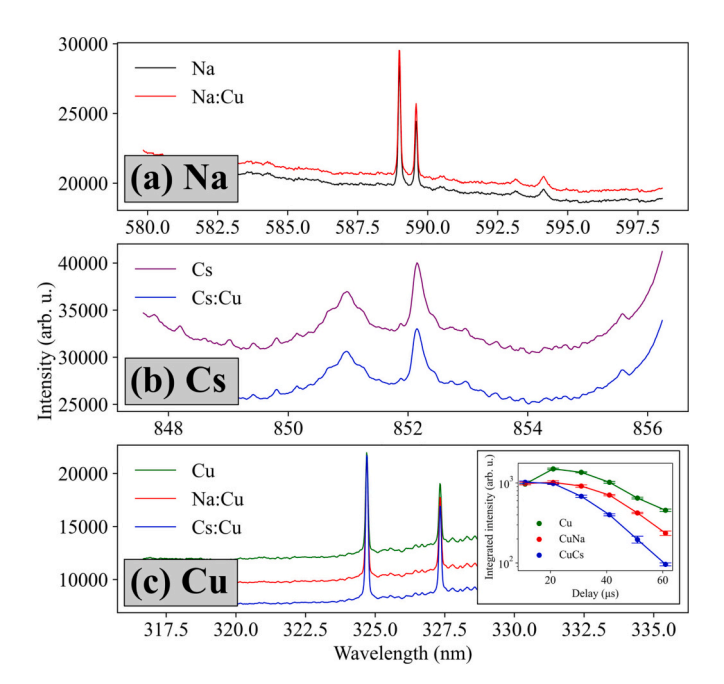


Fig. 3. Early continuum behavior using ns-LIBS with (delay/width) of (1/10) μ s near (a) Na, (b) Cs, and (c) Cu doublet emissions. Inset of (c) shows emission reduction of Cu I emission at 524.754 nm with the addition of Na and Cs.

Table 2Spectroscopic information for Ti emission lines used to generate Boltzmann plots.

λ (nm).	E_u (eV)	Lower term	Upper term
482.041	4.07	$^{1}G_{4}$	${}^{1}F_{3}^{0}$
484.087	3.46	$^{1}D_{2}$	$^{1}D_{2}^{o}$
485.601	4.81	$^{3}H_{6}$	³ I ₇ ^o
498.173	3.34	⁵ F ₅	${}^{5}G_{6}^{o}$
499.107	3.32	$^{5}F_{4}$	$^{5}G_{5}^{o}$
499.950	3.31	⁵ F ₃	${}^{5}G_{4}^{o}$
500.721	3.29	$^{5}F_{2}$	${}^{5}G_{3}^{o}$
517.374	2.40	$^{3}F_{2}$	${}^{3}F_{2}^{0}$
519.297	2.41	$^{3}F_{3}$	${}^{3}F_{3}^{0}$
521.038	2.43	$^{3}F_{4}$	${}^{3}F_{4}^{0}$

temperatures are obtained with 10 μs gate widths, with gate delays incremented using 10 μs steps starting from 10 μs and stopping at 50 μs . Transition probabilities are assigned a $\pm 50\%$ error during error propagation calculations. Boltzmann plots are provided in Fig. 4(a) for Ti and 4(b) for Al:Ti, where all R^2 values are greater than 0.97.

Using the temperatures from the Boltzmann plots, electron densities n_e are determined using the Stark broadening method for Al I at 396.152 nm. The electron density is calculated using Eq. (1) where the electron-impact half-width parameter w is interpolated between 0.0134 nm at 5,000 K and 0.0154 nm at 10,000 K [44].

$$\Delta \lambda_{Stark} = 2w \frac{n_e}{10^{16}} \tag{1}$$

The Stark width is determined by extracting the Lorentzian FWHM contribution from the total FWHM of the fitted profile through an empirical formula with less than 1 % error and subtracting the instrumental broadening contribution [45]. Doppler broadening is calculated to be approximately 0.003 nm at 6,500 K such that its contribution is negligible compared to the total FWHM of the 396.152 nm line which is on the order of 0.1 nm. The temperature cannot be determined for the non-binary Al aerosol, so the same temperatures as Ti is assumed when assigning a value for w. While it is likely that the Al aerosol will experience a different temperature as the Ti aerosol due to differences in thermophysical properties of the aerosol constituents, it is noted that w is weakly dependent on the plasma temperature such that every 1,000 K increase corresponds to less than a 3% difference in w.

The plasma temperature is shown to steadily decrease with time in Fig. 4(c) as the plasma cools for both Ti and Al:Ti aerosols. The binary Al:Ti aerosol achieves a higher temperature, especially at the earlier stages of the plasma where differences in the temperature exceeds 700 K at 20 μ s. A similar decrease in temperature using emissions from Lu II for particles containing Al, Cu, Lu, and Mn was previously reported by Asgill et al. [29], but the study also showed a negligible change in temperature with the addition of Na to the particle matrix. While the exact reason for this discrepancy is unclear, it is likely that temperatures derived using Boltzmann plots for Lu II (three transitions used are at 339.71 nm, 350.74 nm, and 355.44 nm) are prone to larger variances for several reasons including the weaker emission strength of Lu II compared to Ti I, interference caused by N2 emissions near the wavelength region at later times, and the lack of transitions at lower upper energy levels given the 5.23 eV ionization threshold of Lu I. This may result in a change to the plasma temperature that is statistically indiscernible. It is also noted that the presented results here disagrees with the temperature trends reported by Diwakar et al. [27] which showed an increase in local plasma temperature from 2–40 μs attributed to the gradual transfer of heat from the plasma into the particle during dissociation. The authors used ionic and neutral emissions from both Mg and Cd which were used to construct a Saha-Boltzmann relation that is independent of the electron density [46]. However, this assumes complete atomization and equal electron densities for Mg and Cd which may not be the case in a LPP,

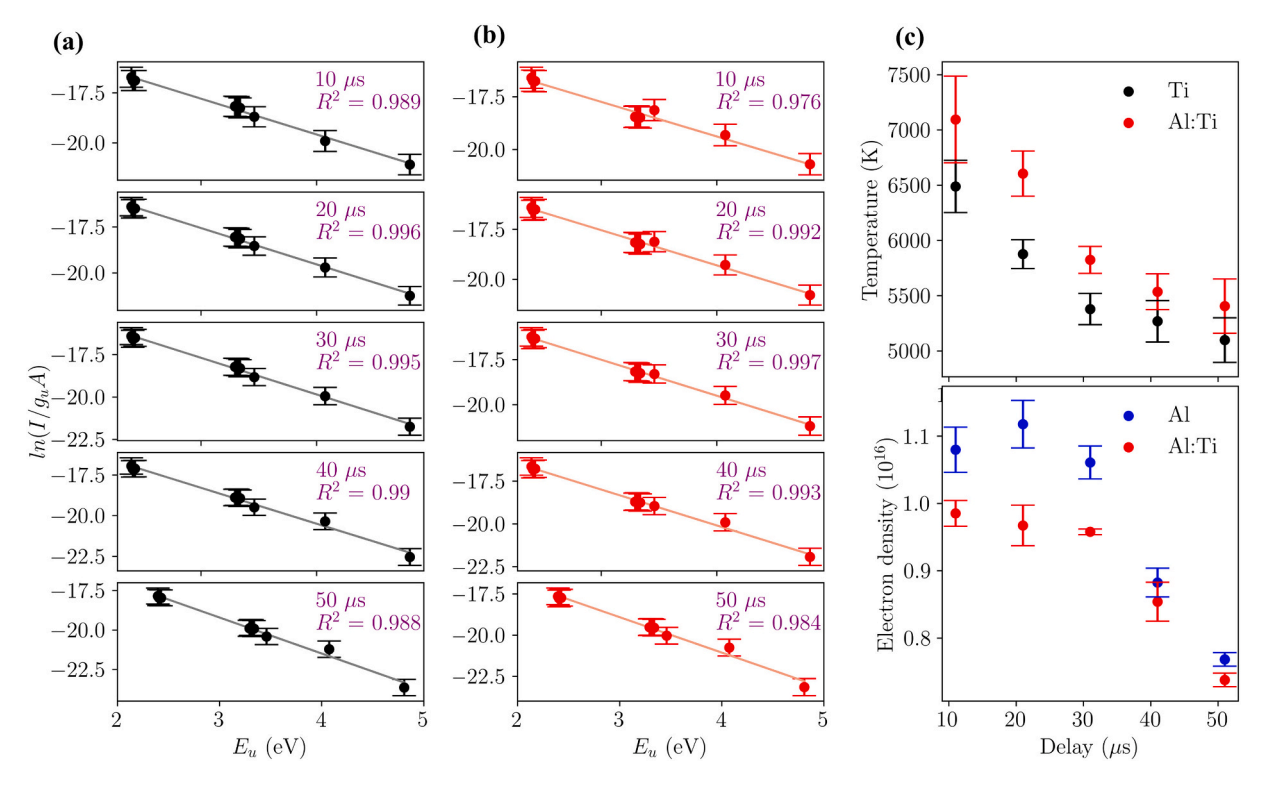


Fig. 4. Boltzmann plots for (a) Ti and (b) Al:Ti obtained with $10 \mu s$ gate widths, with gate delays incremented using $10 \mu s$ steps starting from $11 \mu s$ and stopping at $51 \mu s$. The temperature and electron densities are shown in (c), where the $396.152 \mu s$ m Al I line is used to determine the electron density using the Stark broadening method.

with the original implementation of the technique targeting ICPs in a pure Ar atmosphere.

The electron density determined for the Al:Ti aerosol is lower compared to the Al aerosol by more than 10%. These findings are considered in the context of Saha's equation given in Eq. (2)[47].

$$\frac{n_{\rm II}}{n_{\rm I}} = 2 \frac{Z_{\rm II}(T)}{Z_{\rm I}(T)} n_e^{-1} \left(\frac{2\pi m_e kT}{h^2} \right)^{3/2} \exp\left(-\frac{E_{\rm ion}}{kT} \right)$$
 (2)

Here, the subscript II indicates the ions of a given species and the subscript I indicates the neutral atoms, the population densities being denoated by $n_{\rm II}$ and $n_{\rm I}$, respectively. The ion-to-neutral ratio is inversely proportional to electron density, and thus the decrease in electron density of Al:Ti compared to Al is interpreted as an increase to the ion-to-neutral ratio. As such, given the highest decrease in electron density of 14% at 20 μ s in Fig. 4(c), an expected increase of no more than 14% to the ion-to-neutral ratio can be expected for any given temperature. However, an increase in temperature also imparts a higher ion-to-neutral ratio which may dominate the contributions from n_e . A closer examination is necessary given the values of the partition function are not intuitively understood. As such, the fractional change in $(n_{\rm II}/n_{\rm I})$ is determined using Eq. (3) for Ti using the temperatures in Fig. 4(c).

$$\frac{(n_{\rm II}/n_{\rm I})_{\rm Al:Ti}}{(n_{\rm II}/n_{\rm I})_{\rm Ti}} = \frac{[Z_{\rm II}(T)/Z_{\rm I}(T)]_{\rm Al:Ti}}{[Z_{\rm II}(T)/Z_{\rm I}(T)]_{\rm Ti}} \left(\frac{T_{\rm Al:Ti}}{T_{\rm Ti}}\right)^{3/2} \exp\left[\frac{-E_{\rm ion}}{k} \left(\frac{1}{T_{\rm Al:Ti}} - \frac{1}{T_{\rm Ti}}\right)\right]$$
(3)

It is also noted that Eqs. (2) and (3) are both dependent on the ionization threshold $E_{\rm ion}$ of the element which is 6.828 eV for Ti. As shown in Fig. 5, the observed changes in plasma temperature ΔT more significantly increases the ion-to-neutral ratio compared to the observed changes in electron density Δn_e . Larger standard deviations are incurred by temperature compared to electron density as error propagation is carried out for Eq. (3), but temperature still shows a consistently higher mean increase to the ion-to-neutral ratio with absent overlap at one standard deviation at 10 μ s and 20 μ s.

Compared to a previous study by Judge et al., changes in the electron

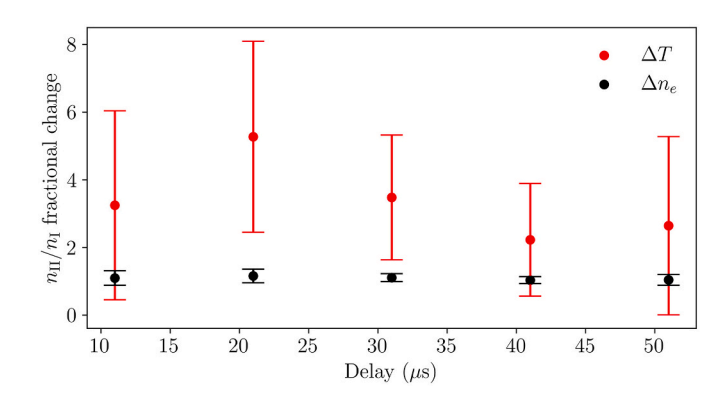


Fig. 5. Increase in ion-to-neutral ratio with observed changes in plasma temperature ΔT and electron density Δn_e shown in Fig. 4(c). Temperature changes are calculated using Eq. (3).

density are not found to be as significant as the changes in the plasma temperature in relation to increasing the ion-to-neutral ratio and any subsequent recombination [30]. In their work, they simulate experimental Na and Mg peaks using ATOMIC under LTE conditions with constant plasma temperatures and mass densities. The electron density was simulated to change by approximately a factor of 2.4 between a pure Na pressed pellet and a Na:Cu pressed pellet with a molar fraction of 1:9 which was speculated to lead to greater neutral atom recombination. A factor of 2.4 increase to the ion-to-neutral ratio is supported to be possible as shown in Fig. 5, however a majority of the contribution is determined to be from changes in the plasma temperature. In their case, it is likely that fixing the plasma temperature for all simulated measurements overestimates changes in electron density in order to compensate the absent contributions from temperature changes. However, it is also possible that temperature changes are more prominent for aerosols due to the thermal process of plasma-particle interactions driving particle dissociation [34].

The current results indicate that signal enhancement observed for Na resonance emissions with Cu present can be driven by temperature changes which increases neutral atom recombination. However, the reduction in emission observed for Cs and Cu is not explained. In order to gain better insight, the elemental fractionation behavior is analyzed for Ti I for the emission lines listed in Table 2. The elemental fractionation behavior is shown in Fig. 6(a) ordered by transition wavelengths. Surprisingly, elemental fractionation behavior is shown to change for each transition as transitions observed in the 484 nm region are consistently enhanced whereas transitions in the 501.5 nm and 520 nm regions show reduction at early times. In particular, the transitions selected in the 501.5 nm and 520 nm region share similar fractionation ratios whereas those in the 484 nm region are seemingly uncorrelated. The transitions in the 501.5 nm region all arise from the same ${}^5G_6^0$ - 5F_4 terms and multiplet, as shown in Table 2. Likewise, the transitions in the 520 nm region share the same ${}^{3}F_{4}$ - ${}^{3}F_{4}^{0}$ terms and multiplet, indicating that elemental fractionation characteristics are particular to the electron configuration. Conversely, the transitions in the 484 nm region all arise from different electron configurations such that fractionation behaviors are not shared.

Ordering the Ti I transitions based on upper energy levels as in Fig. 6 reveals higher upper energy levels have a tendency to be enhanced with Al present. Naturally, transitions with higher upper energy levels are most prominent at higher plasma temperatures. Based on the temperature trend shown in Fig. 4(a), it is likely that the temperature difference between Ti and Al:Ti is reduced at later times as both converge towards the ambient temperature. As such, transitions with higher upper energy levels are more prone to signal enhancement as they occur when

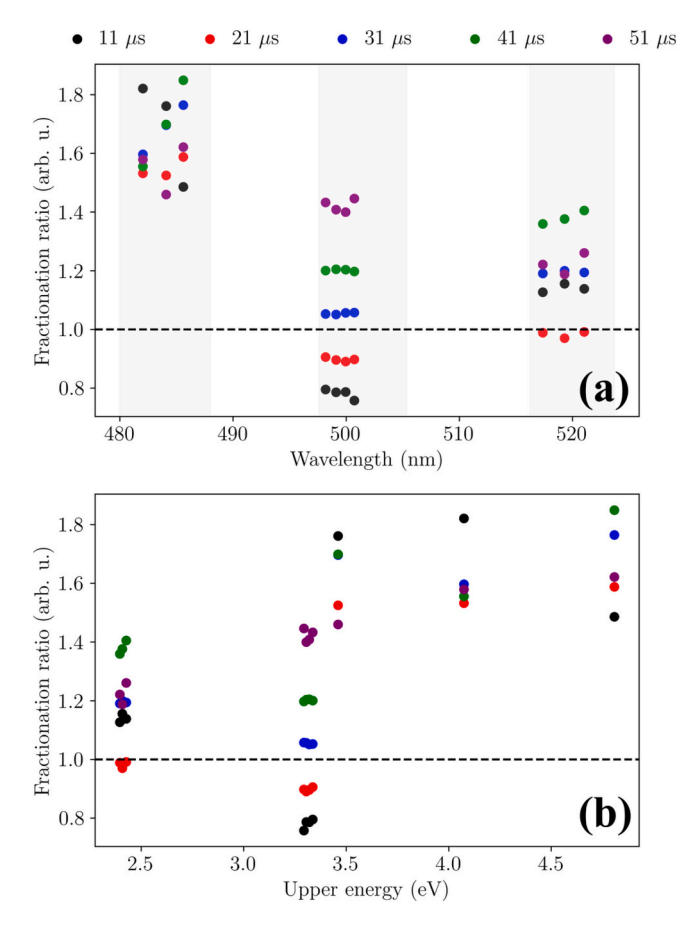


Fig. 6. Elemental fractionation of Ti I ordered by (a) wavelength and (b) upper energy level of transition. Grayed wavelength regions in (a) shows spectral regions measured containing Ti I lines centered at 484, 501.5, and 520 nm.

temperature differences are the highest during the early stages of the plasma. This would also explain why Diwakar et al. in [27] and Judge et al. in [30] observed fractionation ratios approach unity at later times, since the temperature difference would gradually be reduced leading to similarly populated Na I upper energy levels between Na and Na:Cu particle matrices. The population shift towards higher upper energy levels and ion-to-neutral ratios would consequently reduce emissions that arise from lower upper energy levels in the early stages of the plasma. This is roughly seen in Fig. 6(b) for the transitions near 2.4 eV and 3.3 eV corresponding to the the transitions in the 501.5 nm and 520 nm regions in 6(a), as the signal is first reduced early on and subsequently enhancement at later times. This behavior is also demonstrated in Fig. 7 for Al I at 396.152 nm with an upper energy level of 3.143 eV, which shares a similar upper energy level to the Ti I ${}^5G_6^o$ - 5F_4 transitions in the 501.5 nm region near 3.3 eV. Both show an initial reduction in emission followed by enhancement at later times which corresponds to the gradual increase in the upper energy level population as the plasma cools.

Elemental fractionation is evidenced to be largely temperature driven which induces a shift in both energy levels and ion-to-neutral ratios. Thus, enhancement and reduction of emission signals is highly dependent on the exact energy level structure of the element where similar energy levels can give rise to similar fractionation trends which is seen between the same element using Ti with transitions within the same multiplet in Fig. 6 and with different elements such as Al and Ti in Fig. 7 with close upper energy levels. This explanation also agrees with the observed signal enhancement for Na and the signal reduction for Cs in Fig. 2 as the upper energy level of the resonance transition for Cs (1.455 eV) is lower compared to Na (2.104 eV). Furthermore, this indicates that fs-LIBS incurs smaller changes in the plasma temperature between different particle loads which would reduce the effects of elemental fractionation. We also note that while some transitions including the Ti I ${}^5G_6^0$ - 5F_4 multiplet transitions (Fig. 7) show a smooth transition from signal reduction to gradual signal enhancement at later times, other transitions show sporadic changes in the average fractionation ratio as the plasma cools. An example is clearly shown with Na and Cs in Fig. 2(a), where the exact fractionation ratio appear to arbitrarily increase and decrease with time. Similarly, some Ti I transitions in Fig. 6 (a) show similar fluctuations with time. At this point, exact changes to the fractionation ratio remains difficult to predict especially given the inhomogeneity in plasma temperatures with exact spatial origins of particle emissions being unknown.

At later times, molecular emission from TiO and AlO are visible such that fractionation of molecular species can be studied. For TiO, the $\Delta\nu=0$ branch of the γ band is measured using a 50 μs gate delay and a 200 μs gate width. The $\Delta\nu=0$ branch of the $B^2\Sigma^+{\to}X^2\Sigma^+$ band for AlO is measured using a 50 μs gate delay and a 500 μs gate width [48]. The measurements presented in Fig. 8 indicate that elemental fractionation

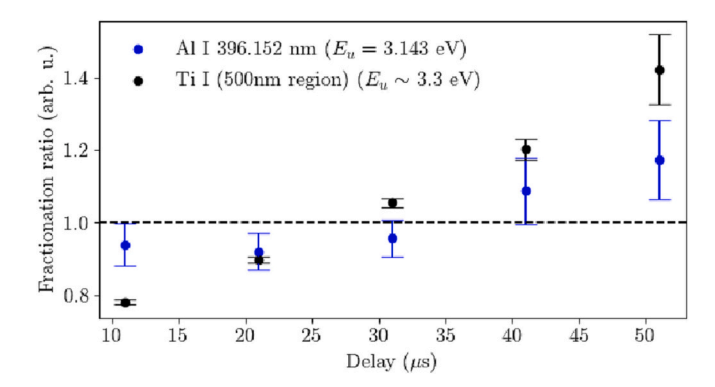


Fig. 7. Elemental fractionation of Al I at 396.152 nm with Ti present, and of Ti I $^5G_6^\circ$ - 5F_4 transitions near 500 nm with Al present.

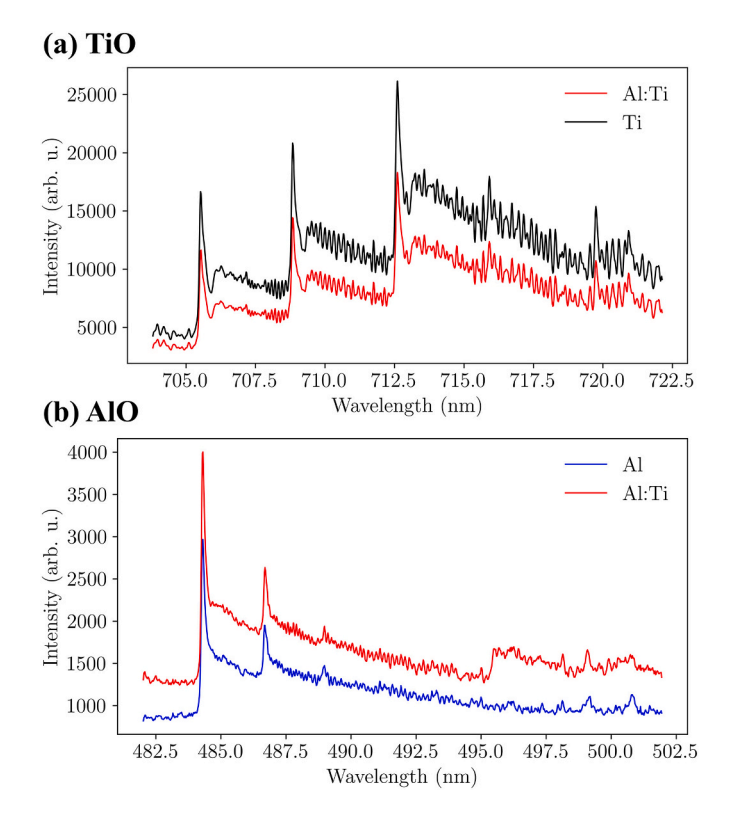


Fig. 8. Elemental fractionation of (a) TiO γ band with Al present and (b) AlO $B^2\Sigma^+ \rightarrow X^2\Sigma^+$ band with Ti present.

is present in molecular emissions similar to atomic emissions.

For the current case of Al and Ti mixtures, it is shown that the AlO emissions are enhanced whereas the TiO emission are reduced which may be indicative of competing reaction pathways. While O atoms are relatively abundant compared to the low molar concentrations of Al and Ti, the localized nature of plasma-particle interactions can potentially emphasize the local abundance of O atoms relative to the reactant analytes. The AlO emission measured by Hartig et al. was shown to increase with partial pressure under a O_2 atmosphere, indicating reactions are primarily limited by both collision rates and availability of O_2 reactants [49]. This also indicates that elemental fractionation of neutral atoms is affected not only by temperature changes in the plasma, but to some extent by reactions with gas species in air. Previous studies have also observed C I emissions from graphite and coal samples to be reduced in N_2 -rich atmospheres which is attributed to increased reaction rates to form C bonding molecules [50,51].

While the current experiments cannot determine the relative contribution of molecular formation towards elemental fractionation trends in neutral atoms, it can be assumed that molecular formation would be a late-stage contributor as the early difference in the plasma temperature induced by multi-element particle matrices is gradually deemphasized. Given emissions from Na and Cs persist beyond 300 µs in Fig. 8 and the highly reactive nature of free alkali metal atoms in air, it is safe to assume chemical kinetics must be considered as a source of elemental fractionation for long-gated LIBS measurements. However, the current experiments do not investigate the spatiotemporal dependence of molecular emissions within the LPP that are known to exist for AlO and other molecules which likely influences molecular fractionation [52–55]. For the Cs and Na experiments, changing the position of the collection lens was observed to change the fractionation ratio. This indicates that fractionation behavior in the LPP is spatially dependent, which given the importance of temperature on elemental fractionation, is intuitively understood to arise from observing plasma-particle interactions within different temperature regions of the LPP. Further experiments are required to better understand the spatial dependence of atomic and molecular fractionation which is not conducted at this time.

4. Conclusion

The origins of elemental fractionation in aerosol LIBS has been investigated for the purpose of detecting multi-element airborne fallout particle. Despite similar the chemical properties between Cs and Na, the presence of Cu in the particle matrix was shown to enhance the Na I resonance emissions while reducing the emissions from Cs I while performing LIBS. Implementing fs-LIBS revealed similar trends in elemental fractionation, but the fractionation ratio relative to ns-LIBS was significantly reduced in most cases by more than 50%. These results provide motivation to develop the pedigree of fs-LIBS through future aerosol research as currently the use of fs-pulses for aerosol LIBS measurements remain sparse. In the current study, elemental fractionation is determined to be driven by changes in the plasma temperature induced by different aerosol compositions. Furthermore, Ti I transitions of the same multiplet are shown to share the same fractionation ratios at different times during the plasma evolution which indicates fractionation behavior is dependent on the energy level structure of the element. Transitions with higher upper energy levels were consistently enhanced between 10-60 µs, whereas transitions with lower upper energy levels showed early signal reduction followed by weak signal enhancement at later times past 30 µs. Elemental fractionation is thus evidenced to be caused by a shift towards higher upper energy states and ion-to-neutral population ratios in the early stages of the plasma where changes to the electron density had a marginal influence in comparison. While broad signal enhancement and signal reduction trends are observed based on upper energy levels of emission transitions, the average fractionation ratio is shown to fluctuate with time and remain difficult to predict. Developing further insight into the effects of plasma inhomogeneity on particle emissions may narrow down the origins of elemental fractionation by accounting for changing local plasma conditions.

The molecular emission from TiO and AlO were also shown to undergo fractionation, where AlO emissions were enhanced with Ti present and TiO emission were reduced with Al present. While current measurements cannot determine the exact reason behind the observed changes in molecular emissions, it is speculated that molecular formation can influence elemental fractionation at later stages of the plasma as neutral atoms are depleted through reactions with ambient gas species. Further experiments are required to determine the relative contribution of molecular formation towards elemental fractionation.

CRediT authorship contribution statement

Kyle S. Latty: Conceptualization, Methodology, Software, Validation, Formal-analysis, Investigation, Writing-original-draft, Visualization. **Kyle C. Hartig:** Conceptualization, Methodology, Validation, Resources, Writing-review-editing, Supervision, Project-administration, Funding-acquisition.

Declaration of Competing Interest

The authors declare that they have no known competing financial interests or personal relationships that could have appeared to influence the work reported in this paper.

Data availability

Data will be made available on request.

Acknowledgements

This document is the result of research funded partially by the University of Florida Herbert Wertheim College of Engineering; Department

of Defense Science, Mathematics, and Research for Transformation (SMART) Scholarship-for-Service Program; Department of Energy National Nuclear Security Administration award number DE-NA0003920; National Science Foundation award number CHE1905301; and Defense Threat Reduction Agency award numbers HDTRA1-20–2-0002 and HDTRA1-19–1-0025.

References

- [1] I. Korsakissok, A. Mathieu, D. Didier, Atmospheric dispersion and ground deposition induced by the Fukushima Nuclear Power Plant accident: A local-scale simulation and sensitivity study, Atmos. Environ. 70 (2013) 267–279.
- [2] P.D. Mclaughlin, B. Jones, M.M. Maher, An update on radioactive release and exposures after the Fukushima Dai-ichi nuclear disaster, BJR 85 (2012) 1222–1225.
- [3] G. Steinhauser, A. Brandl, T.E. Johnson, Comparison of the Chernobyl and Fukushima nuclear accidents: A review of the environmental impacts, Sci. Total Environ. 470–471 (2014) 800–817.
- [4] V. Saenko, V. Ivanov, A. Tsyb, T. Bogdanova, M. Tronko, Y. Demidchik, S. Yamashita, The Chernobyl Accident and its Consequences, Clin. Oncol. 23 (2011) 234–243.
- [5] P. Thakur, S. Ballard, R. Nelson, An overview of Fukushima radionuclides measured in the northern hemisphere, Sci. Total Environ. 458–460 (2013) 577–613
- [6] M.D. Bondarkov, B.Y. Oskolkov, S.P. Gaschak, S.I. Kireev, A.M. Maksimenko, N. I. Proskura, G.T. Jannik, E.B. Farfán, Environmental radiation monitoring in the Chernobyl exclusion zone—history and results 25 years after, Health Phys. 101 (2011) 442–485.
- [7] H.L. Beck, B.G. Bennett, Historical overview of atmospheric nuclear weapons testing and estimates of fallout in the continental United States, Health Phys. 82 (2002) 591–608.
- [8] R.C. Chinni, D.A. Cremers, L.J. Radziemski, M. Bostian, Detection of Uranium Using Laser-Induced Breakdown Spectroscopy, Appl. Spectrosc. 63 (2009) 1238–1250.
- [9] M. Burger, L. Finney, L. Garrett, S. Harilal, K. Hartig, J. Nees, P. Skrodzki, X. Xiao, I. Jovanovic, Laser ablation spectrometry for studies of uranium plasmas, reactor monitoring, and spent fuel safety, Spectrochim. Acta Part B: At. Spectrosc. 179 (2021), 106095.
- [10] H.B. Andrews, J. McFarlane, K.G. Myhre, Monitoring Noble Gases (Xe and Kr) and Aerosols (Cs and Rb) in a Molten Salt Reactor Surrogate Off-Gas Stream Using Laser-Induced Breakdown Spectroscopy (LIBS), Appl. Spectrosc. (2022), 000370282210886.
- [11] M. Burger, L. Garrett, A.J. Burak, V. Petrov, A. Manera, P. Sabharwall, X. Sun, I. Jovanovic, Trace xenon detection in helium environment via laser-induced breakdown spectroscopy, J. Anal. At. Spectrom. 36 (2021) 824–828.
- [12] K.C. Hartig, I. Ghebregziabher, I. Jovanovic, Standoff Detection of Uranium and its Isotopes by Femtosecond Filament Laser Ablation Molecular Isotopic Spectrometry, Sci. Rep. 7 (2017) 43852.
- [13] P. Rohwetter, J. Yu, G. Méjean, K. Stelmaszczyk, E. Salmon, J. Kasparian, J.-P. Wolf, L. Wöste, Remote LIBS with ultrashort pulses: Characteristics in picosecond and femtosecond regimes, J. Anal. At. Spectrom. 19 (2004) 437–444.
- [14] V. Hohreiter, D.W. Hahn, Calibration Effects for Laser-Induced Breakdown Spectroscopy of Gaseous Sample Streams: Analyte Response of Gas-Phase Species versus Solid-Phase Species, Anal. Chem. 77 (2005) 1118–1124.
- [15] D.W. Hahn, N. Omenetto, Laser-Induced Breakdown Spectroscopy (LIBS), Part I: Review of Basic Diagnostics and Plasma–Particle Interactions: Still-Challenging Issues Within the Analytical Plasma Community, Appl. Spectrosc. 66 (2010) 335A–366A.
- [16] J.E. Carranza, D.W. Hahn, Assessment of the Upper Particle Size Limit for Quantitative Analysis of Aerosols Using Laser-Induced Breakdown Spectroscopy, Anal. Chem. 74 (2002) 5450–5454.
- [17] E. Vors, L. Salmon, Laser-induced breakdown spectroscopy (LIBS) for carbon single shot analysis of micrometer-sized particles, Anal. Bioanal. Chem. 385 (2006) 281–286.
- [18] C. Papastefanou, A. Ioannidou, S. Stoulos, M. Manolopoulou, Atmospheric deposition of cosmogenic 7Be and 137Cfsrom fallout of the Chernobyl accident, Sci. Total Environ. 6 (1995).
- [19] P. Spezzano, Distribution of pre- and post-Chernobyl radiocaesium with particle size fractions of soils, J. Environ. Radioact. 83 (2005) 117–127.
- [20] B. Shleien, N.A. Gaeta, A.G. Friend, Determination of Particle Size Characteristics of Old and Fresh Airborne Fallout by Graded Filtration, Health Phys. 12 (1966) 633–639.
- [21] A. Kabdyrakova, S. Lukashenko, A. Mendubaev, A. Kunduzbayeva, A. Panitskiy, N. Larionova, Distribution of artificial radionuclides in particle-size fractions of soil on fallout plumes of nuclear explosions, J. Environ. Radioact. 186 (2018) 45–53.
- [22] S. Zhang, M. He, Z. Yin, E. Zhu, W. Hang, B. Huang, Elemental fractionation and matrix effects in laser sampling based spectrometry, J. Anal. At. Spectrom. 31 (2016) 358–382.
- [23] H.-R. Kuhn, D. Günther, Elemental Fractionation Studies in Laser Ablation Inductively Coupled Plasma Mass Spectrometry on Laser-Induced Brass Aerosols, Anal. Chem. 75 (2003) 747–753.
- [24] I. Kroslakova, D. Günther, Elemental fractionation in laser ablation-inductively coupled plasma-mass spectrometry: Evidence for mass load induced matrix effects

- in the ICP during ablation of a silicate glass, J. Anal. At. Spectrom. 22 (2007) 51–62.
- [25] B. Zhang, M. He, W. Hang, B. Huang, Minimizing Matrix Effect by Femtosecond Laser Ablation and Ionization in Elemental Determination, Anal. Chem. 85 (2013) 4507–4511.
- [26] P.K. Diwakar, S.S. Harilal, N.L. LaHaye, A. Hassanein, P. Kulkarni, The influence of laser pulse duration and energy on ICP-MS signal intensity, elemental fractionation, and particle size distribution in NIR fs-LA-ICP-MS, J. Anal. At. Spectrom. 28 (2013) 1420.
- [27] P. Diwakar, P. Jackson, D. Hahn, The effect of multi-component aerosol particles on quantitative laser-induced breakdown spectroscopy: Consideration of localized matrix effects, Spectrochim. Acta Part B: At. Spectrosc. 62 (2007) 1466–1474.
- [28] P.K. Diwakar, P. Kulkarni, Laser Induced Breakdown Spectroscopy for Analysis of Aerosols, in: S. Musazzi, U. Perini (Eds.), Laser-Induced Breakdown Spectroscopy: Theory and Applications, Springer Series in Optical Sciences, Springer, Berlin, Heidelberg, 2014, pp. 227–256, https://doi.org/10.1007/978-3-642-45085-3 9.
- [29] M.E. Asgill, S. Groh, K. Niemax, D.W. Hahn, The use of multi-element aerosol particles for determining temporal variations in temperature and electron density in laser-induced plasmas in support of quantitative laser-induced breakdown spectroscopy, Spectrochim. Acta Part B: At. Spectrosc. 109 (2015) 1–7.
- [30] E.J. Judge, J. Colgan, K. Campbell, J.E. Barefield, H.M. Johns, D.P. Kilcrease, S. Clegg, Theoretical and experimental investigation of matrix effects observed in emission spectra of binary mixtures of sodium and copper and magnesium and copper pressed powders, Spectrochim. Acta Part B: At. Spectrosc. 122 (2016) 142–148.
- [31] N.H. Magee, Los Alamos Opacities: Transition from LEDCOP to ATOMIC, in: AIP Conf. Proc., vol. 730, AIP, Santa Fe, New Mexico (USA), 2004, pp. 168–179, https://doi.org/10.1063/1.1824868.
- [32] F. Théberge, W. Liu, P.T. Simard, A. Becker, S.L. Chin, Plasma density inside a femtosecond laser filament in air: Strong dependence on external focusing, Phys. Rev. E 74 (2006), 036406.
- [33] K.S. Latty, K.C. Hartig, Spatiotemporal plasma-particle characterization of dry aerosols using nanosecond, femtosecond, and filament laser-produced plasmas, Appl. Spectrosc. 0 (0) 00037028221149480.
- [34] V. Hohreiter, D.W. Hahn, Plasma-Particle Interactions in a Laser-Induced Plasma: Implications for Laser-Induced Breakdown Spectroscopy, Anal. Chem. 78 (2006) 1509–1514.
- [35] D.W. Hahn, J.E. Carranza, G.R. Arsenault, H.A. Johnsen, K.R. Hencken, Aerosol generation system for development and calibration of laser-induced breakdown spectroscopy instrumentation, Rev. Sci. Instrum. 72 (2001) 3706–3713.
- [36] J. Carranza, D. Hahn, Sampling statistics and considerations for single-shot analysis using laser-induced breakdown spectroscopy, Spectrochim. Acta Part B: At. Spectrosc. 57 (2002) 779–790.
- [37] D. Diaz, D.W. Hahn, Aerosol measurements with laser-induced breakdown spectroscopy and conditional analysis, Spectrochim. Acta Part B: At. Spectrosc. 179 (2021), 106107.
- [38] A. Kramida, Yu. Ralchenko, J. Reader, and NIST ASD Team, NIST Atomic Spectra Database (ver. 5.10), [Online]. Available:https://physics.nist.gov/asd [2022, November 28]. National Institute of Standards and Technology, Gaithersburg, MD, 2022.
- [39] M.S. Afgan, S. Sheta, Y. Song, W. Gu, Z. Wang, Plasma imaging for physical variations in laser-induced aerosol plasma with particle size increase, J. Anal. At. Spectrom. 35 (2020) 2649–2655.
- [40] B.N. Chichkov, C. Momma, S. Nolte, Femtosecond, picosecond and nanosecond laser ablation of solids, Appl. Phys. A 63 (1996) 109–115.
- [41] E.G. Gamaly, A.V. Rode, B. Luther-Davies, V.T. Tikhonchuk, Ablation of solids by femtosecond lasers: Ablation mechanism and ablation thresholds for metals and dielectrics, Phys. Plasmas 9 (2002) 949–957.
- [42] T.A. Labutin, V.N. Lednev, A.A. Ilyin, A.M. Popov, Femtosecond laser-induced breakdown spectroscopy, J. Anal. At. Spectrom. 31 (2016) 90–118.
- [43] A. De Giacomo, R. Gaudiuso, M. Dell'Aglio, A. Santagata, The role of continuum radiation in laser induced plasma spectroscopy, Spectrochim. Acta Part B: At. Spectrosc. 65 (2010) 385–394.
- [44] H.R. Griem, Spectral Line Broadening by Plasmas, Academic Press Inc., New York, NY, 1974.
- [45] E. Whiting, An empirical approximation to the Voigt profile, J. Quant. Spectrosc. Radiat. Transfer 8 (1968) 1379–1384.
- [46] E. Tognoni, M. Hidalgo, A. Canals, G. Cristoforetti, S. Legnaioli, A. Salvetti, V. Palleschi, Combination of the ionic-to-atomic line intensity ratios from two test elements for the diagnostic of plasma temperature and electron number density in Inductively Coupled Plasma Atomic Emission Spectroscopy, Spectrochim. Acta Part B: At. Spectrosc. 62 (2007) 435–443.
- [47] A. De Giacomo, J. Hermann, Laser-induced plasma emission: From atomic to molecular spectra, J. Phys. D: Appl. Phys. 50 (2017), 183002.
- [48] C.G. Parigger, A.C. Woods, D.M. Surmick, G. Gautam, M.J. Witte, J.O. Hornkohl, Computation of diatomic molecular spectra for selected transitions of aluminum monoxide, cyanide, diatomic carbon, and titanium monoxide, Spectrochim. Acta Part B: At. Spectrosc. 107 (2015) 132–138.
- [49] K. Hartig, B. Brumfield, M. Phillips, S. Harilal, Impact of oxygen chemistry on the emission and fluorescence spectroscopy of laser ablation plumes, Spectrochim. Acta Part B: At. Spectrosc. 135 (2017) 54–62.
- [50] D. Diaz, D.W. Hahn, Plasma chemistry produced during laser ablation of graphite in air, argon, helium and nitrogen, Spectrochim. Acta Part B: At. Spectrosc. 166 (2020). 105800.

- [51] M. Dong, X. Mao, J.J. Gonzalez, J. Lu, R.E. Russo, Time-resolved LIBS of atomic and molecular carbon from coal in air, argon and helium, J. Anal. At. Spectrom. 27 (2012) 2066
- [52] E.R. Wainwright, S.W. Dean, F.C. De Lucia, T.P. Weihs, J.L. Gottfried, Effect of sample morphology on the spectral and spatiotemporal characteristics of laserinduced plasmas from aluminum, Appl. Phys. A 126 (2020) 83.
- [53] E.J. Kautz, P.J. Skrodzki, M. Burger, B.E. Bernacki, I. Jovanovic, M.C. Phillips, S. S. Harilal, Time-resolved imaging of atoms and molecules in laser-produced uranium plasmas, J. Anal. At. Spectrom. 34 (2019) 2236–2243.
- [54] E.J. Kautz, M.C. Phillips, A. Zelenyuk, S.S. Harilal, Oxidation in laser-generated metal plumes, Phys. Plasmas 29 (2022), 053509.
- [55] E.J. Kautz, E.N. Weerakkody, M.S. Finko, D. Curreli, B. Koroglu, T.P. Rose, D. G. Weisz, J.C. Crowhurst, H.B. Radousky, M. DeMagistris, N. Sinha, D.A. Levin, E. L. Dreizin, M.C. Phillips, N.G. Glumac, S.S. Harilal, Optical spectroscopy and modeling of uranium gas-phase oxidation: Progress and perspectives, Spectrochim. Acta Part B: At. Spectrosc. 185 (2021), 106283.